Mechanics of Advanced Composite Structures

Journal homepage: https://macs.semnan.ac.ir/

Semnan University

ISSN: 2423-7043

*Research Article*

# Analytical Modeling of Functionally Graded Carbon Nanotube-Reinforced Composite Plates under Low-Velocity Impact

**Saeid Feli *, Bromand Karimi, Seyed Sajad Jafari**

*Department of Mechanical Engineering, Razi University, Kermanshah, Iran*

**ARTICLE INFO**

***Article history:***

Received: 2023-07-01

Revised: 2023-12-09

Accepted: 2024-02-01

***Keywords:***

Functionally graded;
Carbon nanotube;
Low-velocity;
Impact;
Analytical model.

**ABSTRACT**

In this paper, analytical and numerical modeling has investigated the behavior of Functionally Graded Carbon Nanotube-Reinforced Composite (FG-CNTRC) plates under Low-Velocity Impact (LVI). The mixed law is employed to obtain the mechanical properties of carbon nanotubes (CNT) and methyl methacrylate. Nonlinear equations of analytical modeling are derived based on the Third-order Shear Deformation Theory (TSDT), Hertz law (to define the contact force), and the energy principle. After calculating the strain and stress fields, the Ritz method is used to obtain motion equations. Fourth order Runge-Kutta method is applied for solving equations of motion. In the following, LVI on FG-CNTRC plates is simulated using the FE code, ABAQUS software. The results of the analytical and numerical model are compared with the other results of LVI on FG-CNTRC, and there is good agreement between them. In addition, the effects of CNTs graded profile, volume fraction, impactor velocity, impactor radius, and geometrical parameters are investigated.



## 1. Introduction

Functionally graded carbon nanotubes reinforced composite (FG-CNTRC) structures have widely been used in industrial, aerospace, and ... applications. FG-CNTRCs have good mechanical, thermal, and vibration characteristics properties.

In recent decades, many types of research have been carried out about the behavior of the materials under different loadings, such as impact problems including Low-Velocity Impact (LVI) [1], High-Velocity Impact (HVI)[2, 3], high strain rate loadings[4,5], etc. The projectile velocity is very low so that the strain rate value is less than one so that the behavior of the materials under LVI is nearly similar to the material's response under quasi-static loading. Abrate [4] has studied various models of LVI of the composite and sandwich panel structures which are used in the Hertz contact law. The effect of boundary conditions on LVI on Fiber Metal Laminates (FMLs) is investigated by Zarei et al. [6]. They used Hamilton's principle, Hertzian contact law, and the fourth-order Rung-Kutta method to study and showed the contact duration and the number of contacts between impactor and FMLs will vary when the boundary conditions change.

Taghipoor et al. [7] used the response surface methodology (RSM) to study the impact of graphene nano-sheet, basalt fiber, and polypropylene-grafted maleic anhydride reinforcements on the mechanical behavior of

* **Corresponding author.**
***E-mail address:*** *Felisaeid@gmail.com*

**Cite this article as:**
Feli, S., Karimi, B. and Jafari., S.S., 2024. Analytical Modeling of Functionally Graded Carbon Nanotube-Reinforced Composite Plates under Low-Velocity Impact. *Mechanics of Advanced Composite Structures*, 11(2), pp. 281-294
https://doi.org/10.22075/MACS.2024.31101.1533

polypropylene polymer nanocomposites, experimentally. They showed graphene nano-sheets at 1.5 wt% improved the elastic modulus by about 70%. In addition, Niaraki et al. applied RMS to find the effects of graphene nanosheets, nano clay, and glass fibers on the hybrid polypropylene and ethylene-propylene-monomer (EPDM). According to the results of the article, enhancement of the nanosheets of graphene has improved the elastic modulus.

Taghipoor and Mirzaei [8] studied the effects of the natural kenaf fibers, basalt fiber, and nano-graphene on the tensile strength of the polypropylene-based bio-composites. They showed kenaf fiber has the most effect on improving the tensile strength, and basalt fiber has the most effect on the improvement of the elastic modulus. Sadeghian et al. [9] conducted an experimental study and used optimization to define the absorption and impact strength of fiber-reinforced concrete (FRC).

Lei and Tong [10] analyzed the LVI response of the graphene-reinforced composite functionally graded (GRC-FG) cylindrical shells in thermal environments by using the Halpin–Tsai micromechanical model, Fourier series expansion and Laplace transforms. Fallah et al. [11] presented a semi-analytical model to study the LVI impact response of temperature-dependent CNTRC plates by using the free-mesh Ritz method. They showed the distribution profile of the type X pattern results in lower maximum deflection and higher maximum contact force.

Feli et al. [12] suggested a new analytical model based on the first-order shear deformation theory (FSDT) and spring-mass model for the behavior of CNTRC under LVI. According to the analytical model, by increasing the CNTs volume fraction, enhancement of the axial stress and reduction of the axial strain has occurred.

Yang and Ma [13] analyzed the LVI response of an FG-CNTRC plate with negative Poisson ratios. They combined Reddy's higher-order shear deformation theory, the rule of a mixture model, and the Hertz contact law to derive the equations of motion, material properties, and contact force, respectively. They showed that temperature, initial impact velocity, and contact force increase are effective parameters for FG-CNTRC behavior.

In this paper, the LVI nonlinear response of an FG-CNTRC plate is calculated by analytical and numerical methods. Four different kinds of nanotube distribution layers (i.e., UD, FGV, FGX, and FGO) are studied in the analysis. The mechanical properties of the plate are estimated by using the mixed law. Third-order Shear Deformation Theory (TSDT), Hertz law, and the energy principle are used in the equations of motion. Finally, the fourth-order Runge-Kutta method is used to solve equations of motion. In addition, the numerical method is employed to investigate the behavior of the FG-CNTRC plate under LVI. The results of the analytical and numerical methods are compared with the other well-known models and there is good agreement between them. The effects of CNRTC types, volume fraction, initial velocity, and radius impactor are investigated.

## 2. Analytical Model

The schematic view of LVI on a rectangular FG-CNTRC plate is shown in Figure 1. The length, width, and thickness of the plate are defined as $a$, $b$ and $h$, respectively. In addition, the radius and initial velocity of the spherical rigid impactor are designated as $R$ and $V_0$, respectively.

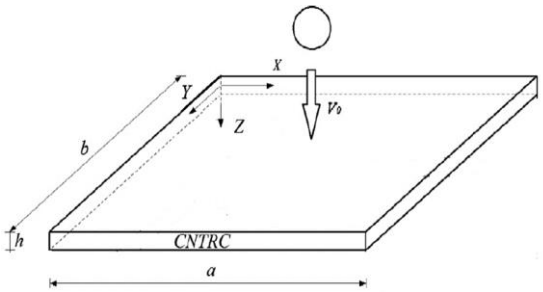


**Fig. 1.** Configuration of an FG-CNTRC plate subjected to LVI.

The principal energy method was employed to derive equations of motion. By considering the plate and impactor as a system, the total potential energy ($P$) and kinematic energy ($T$) of the system can be expressed as:

$$P = \frac{1}{2}\int_V \left(\sigma_{xx}\varepsilon_{xx} + \sigma_{yy}\varepsilon_{yy} + \sigma_{xy}\gamma_{xy} + \sigma_{yz}\gamma_{yz} + \sigma_{xz}\gamma_{xz}\right)dV + \frac{2}{5}K_{imp}\left(y - w_0\left(\frac{a}{2},\frac{b}{2},t\right)\right)^{\frac{5}{2}} \quad (1)$$

$$T = \frac{1}{2}\int_V \rho(\dot{u}^2 + \dot{v}^2 + \dot{w}^2)dV + \frac{1}{2}M_{imp}\dot{y}^2 \quad (2)$$

where $\sigma_{xx}$ and $\sigma_{yy}$ are components of axial plane stress in the x and y direction, respectively. In addition, $\sigma_{yz}$ and $\sigma_{xz}$ are transverse components of the stress field. $\varepsilon_{xx}$ and $\varepsilon_{yy}$ are components of axial strain and $\gamma_{xy}$, $\gamma_{yz}$ and $\gamma_{xz}$ are components of the shear strain field. It is worth mentioning, in the above equation $\left(\frac{a}{2},\frac{b}{2}\right)$

is the position in which impact takes place, $y$ the displacement of the impactor, $w_0$ is transverse displacement of the mid-plane, and $K_{imp}$ the contact stiffness which is evaluated by [14]:

$$K_{imp} = \frac{4}{3}\sqrt{R}\left(\frac{1}{E_{33,imp}} + \frac{1-{\nu_s}^2}{E_s}\right)^{-1} \tag{3}$$

in the above equation, $R$ , $E_{33,imp}$ , $\nu_s$ and $E_s$ are impactor radius, the transverse elasticity modulus in the surface of FG-CNTRC plate, Poisson ratio, and Young modulus of the impactor, respectively. It should be noted that the first and second parts in Eq.(1) demonstrate the potential energy of the plate and potential energy due to contact between the impactor and the plate.

In Eq.(2), $\dot{u}$ , $\dot{v}$ , $\dot{w}$ are components of plate velocity in x, y, and z directions, respectively. In addition, $\rho$ is plate density and impactor velocity. The first part of Eq.(2) represented the kinetic energy of the plate and the second part showed the kinematic energy of the impactor.

To calculate the potential and kinetic energy, the stress and strain field and velocity component (due to displacement) must be defined. High-order Shear Deformation Theory (HSDT) is employed to determine the total displacements ($u$ , $v$ , $w$) along the three coordinate axes ($x$ , $y$ , $z$ ) [15]:

$$\begin{aligned} u(x,y,z,t) &= u_0(x,y,t) - z\frac{\partial w}{\partial x} \\ &\quad + f(z)\theta_1(x,y,t) \\ v(x,y,z,t) &= v_0(x,y,t) - z\frac{\partial w}{\partial y} \\ &\quad + f(z)\theta_2(x,y,t) \\ w(x,y,z,t) &= w_0(x,y,t) \end{aligned} \tag{4}$$

in which ($u_0$ , $v_0$ , $w_0$) are the displacement components along the ($x$ , $y$ , $z$ ) direction, of a point on the midplane, respectively. $\theta_1$ and $\theta_2$ represent rotations of a point on the midplane of the plate, while $f(z) = z\left(1 - \frac{4}{3}\left(\frac{z}{h}\right)^2\right)$ represents the transverse shear strain distribution along the thickness.

The strain-displacement relation of any point of the plate and the stress-strain relation is present may be written as [16]:

$$\begin{aligned} \begin{Bmatrix} \varepsilon_{xx} \\ \varepsilon_{yy} \\ \gamma_{xy} \end{Bmatrix} &= \begin{Bmatrix} \frac{\partial u_0}{\partial x} \\ \frac{\partial v_0}{\partial y} \\ \frac{\partial u_0}{\partial y} + \frac{\partial v_0}{\partial x} \end{Bmatrix} - z\begin{Bmatrix} \frac{\partial^2 w_0}{\partial x^2} \\ \frac{\partial^2 w_0}{\partial y^2} \\ 2\frac{\partial^2 w_0}{\partial xy} \end{Bmatrix} \\ &\quad + f(z)\begin{Bmatrix} \frac{\partial \theta_1}{\partial x} \\ \frac{\partial \theta_2}{\partial y} \\ \frac{\partial \theta_1}{\partial y} + \frac{\partial \theta_2}{\partial x} \end{Bmatrix} \end{aligned} \tag{5}$$

$$\begin{Bmatrix} \gamma_{yz} \\ \gamma_{xz} \end{Bmatrix} = f'(z)\begin{Bmatrix} \theta_2 \\ \theta_1 \end{Bmatrix} \tag{6}$$

$$\begin{Bmatrix} \sigma_{xx} \\ \sigma_{yy} \\ \sigma_{xy} \end{Bmatrix} = \begin{bmatrix} \bar{Q}_{11} & \bar{Q}_{12} & \bar{Q}_{16} \\ \bar{Q}_{12} & \bar{Q}_{22} & \bar{Q}_{26} \\ \bar{Q}_{16} & \bar{Q}_{26} & \bar{Q}_{66} \end{bmatrix}\begin{Bmatrix} \varepsilon_{xx} \\ \varepsilon_{yy} \\ \gamma_{xy} \end{Bmatrix} \tag{7}$$

$$\begin{Bmatrix} \sigma_{yz} \\ \sigma_{xz} \end{Bmatrix} = \begin{bmatrix} \bar{Q}_{44} & \bar{Q}_{45} \\ \bar{Q}_{45} & \bar{Q}_{55} \end{bmatrix}\begin{Bmatrix} \gamma_{yz} \\ \gamma_{xz} \end{Bmatrix} \tag{8}$$

in which $\{\sigma\}$ and $\{\varepsilon\}$ represent the stress and strain components. Besides, the reduced stiffness matrix for the plate and defined below:

$$\begin{aligned} \bar{Q}_{11} &= \frac{E_{11}}{1-\nu_{12}\nu_{21}} \\ \bar{Q}_{22} &= \frac{E_{22}}{1-\nu_{12}\nu_{21}} \\ \bar{Q}_{12} &= \frac{\nu_{21}E_{11}}{1-\nu_{12}\nu_{21}} \\ \bar{Q}_{16} &= \bar{Q}_{26} = \bar{Q}_{45} = 0 \\ \bar{Q}_{66} &= G_{12} \\ \bar{Q}_{44} &= G_{23} \\ \bar{Q}_{55} &= G_{13} \end{aligned} \tag{9}$$

where $E_{ii}\,(i=1,2)$, $\nu_{ij}\,(i,j=1,2)$ and $G_{ij}\,(i,j=1,2,3)$ are Young's modulus, Poisson's ratio, and shear modulus of the FG-CNTRC plate by combining the properties of the matrix (shown by m superscript) and carbon nanotubes (shown by CN superscript). These parameters are determined by the following relations[15]:

$$\begin{aligned} E_{11} &= \eta_1 V_{CN} E_{11}^{CN} + V_m E^m \\ \frac{\eta_2}{E_{22}} &= \frac{V_{CN}}{E_{22}^{CN}} + \frac{V_m}{E^m} \\ \frac{\eta_3}{G_{12}} &= \frac{V_{CN}}{G_{12}^{CN}} + \frac{V_m}{G^m} \\ \nu_{12} &= V_{CN}\upsilon_{12}^{CN} + V_m\upsilon^m \\ \rho &= V_{CN}\rho^{CN} + V_m\rho^m \end{aligned} \tag{10}$$

The coefficients $\eta_i\,(i=1,2,3)$ are introduced to account for the scale-dependent material properties. Furthermore, $V_{CN}$ and $V_m$ are the volume fractions of CNTs and matrix phase, respectively, and must satisfy the bellow condition:

$$V_{CN}+V_m=1 \tag{11}$$

By considering Eqs. (1-9), the potential and kinetic energy can be expressed as below:

$$\begin{aligned}P=\frac{1}{2}\int_V\Bigg(&\bar{Q}_{11}\left[\frac{\partial u_0}{\partial x}-z\frac{\partial^2 w_0}{\partial x^2}+f(z)\frac{\partial\theta_1}{\partial x}\right]^2\\&+2\bar{Q}_{12}\left[\frac{\partial u_0}{\partial x}-z\frac{\partial^2 w_0}{\partial x^2}+f(z)\frac{\partial\theta_1}{\partial x}\right]\left[\frac{\partial v_0}{\partial y}-z\frac{\partial^2 w_0}{\partial y^2}+f(z)\frac{\partial\theta_2}{\partial y}\right]\\&+\bar{Q}_{22}\left[\frac{\partial v_0}{\partial y}-z\frac{\partial^2 w_0}{\partial y^2}+f(z)\frac{\partial\theta_2}{\partial y}\right]^2\\&+\bar{Q}_{66}\left[\frac{\partial u_0}{\partial y}+\frac{\partial v_0}{\partial x}-2z\frac{\partial^2 w_0}{\partial xy}+f(z)\frac{\partial\theta_1}{\partial y}+f(z)\frac{\partial\theta_2}{\partial x}\right]^2+\bar{Q}_{44}[f'(z)\theta_2]^2\\&+\bar{Q}_{55}[f'(z)\theta_1]^2\Bigg)dV+\frac{2}{5}K_{imp}\big(y-w_0(a.b,t)\big)^{\frac{5}{2}}\end{aligned} \tag{12}$$

$$T=\frac{1}{2}\int_V\rho\left(\left[\dot{u}_0-z\frac{\partial\dot{w}_0}{\partial x}+f(z)\dot{\theta}_1\right]^2+\left[\dot{v}_0-z\frac{\partial\dot{w}_0}{\partial y}+f(z)\dot{\theta}_2\right]^2+[\dot{w}_0]^2\right)dV+\frac{1}{2}M_{imp}\dot{y}^2 \tag{13}$$

In the above equations, five parameters are undefined which include: $u_0(x,y,t)$, $v_0(x,y,t)$, $w_0(x,y,t)$, $\theta_1(x,y,t)$ and $\theta_2(x,y,t)$. There are several methods to solve partial or ordinary equations [16-18]. In the paper, the Ritz method is employed. separation of variables method is the first step for solving the equations:

$$\begin{aligned}u_0(x,y.t)&=\sum_{n=1}^{N}U_n(t)N_n^u(x.y)\\v_0(x,y.t)&=\sum_{n=1}^{N}V_n(t)N_n^v(x.y)\\w_0(x,y.t)&=\sum_{n=1}^{N}W_n(t)N_n^w(x.y)\\\theta_1(x,y.t)&=\sum_{n=1}^{N}X_n(t)N_n^{\theta_1}(x.y)\\\theta_2(x,y.t)&=\sum_{n=1}^{N}Y_n(t)N_n^{\theta_2}(x.y)\end{aligned} \tag{14}$$

where, and $Y_n(t)$ are time-dependent coefficients. In addition, $N_n^u$ , $N_n^v$, $N_n^w$ , $N_n^{\theta_1}$ and $N_n^{\theta_2}$ are the shape functions have to be chosen according only to the essential boundary conditions. In this paper, the linear types of shape functions are used (Appendix A). Furthermore, $N$ the number of terms should be chosen to ensure the convergence of the total displacements. By considering Eq (12-13) and appendix:

$$
\begin{aligned}
P = \frac{1}{2}\int_V \Bigg( & \bar{Q}_{11}\left[\sum_{n=1}^{N} U_n(t)\frac{dN_n^u(x.y)}{dx} - z\sum_{n=1}^{N} W_n(t)\frac{d^2N_n^w(x.y)}{dx^2} + f(z)\sum_{n=1}^{N} X_n(t)\frac{dN_n^{\theta_1}(x.y)}{dx}\right]^2 \\
& + 2\bar{Q}_{12}\left[\sum_{n=1}^{N} U_n(t)\frac{dN_n^u(x.y)}{dx} - z\sum_{n=1}^{N} W_n(t)\frac{d^2N_n^w(x.y)}{dx^2} + f(z)\frac{\partial\theta_1}{\partial x}\right]\left[\sum_{n=1}^{N} V_n(t)\frac{dN_n^v(x.y)}{dy}\right. \\
& \left. - z\sum_{n=1}^{N} W_n(t)\frac{d^2N_n^w(x.y)}{dy^2} + f(z)\sum_{n=1}^{N} Y_n(t)\frac{dN_n^{\theta_2}(x.y)}{dy}\right] \\
& + \bar{Q}_{22}\left[\sum_{n=1}^{N} V_n(t)\frac{dN_n^v(x.y)}{dy} - z\sum_{n=1}^{N} W_n(t)\frac{d^2N_n^w(x.y)}{dx^2} + f(z)\sum_{n=1}^{N} Y_n(t)\frac{dN_n^{\theta_2}(x.y)}{dy}\right]^2 \\
& + \bar{Q}_{66}\left[\sum_{n=1}^{N} U_n(t)\frac{dN_n^u(x.y)}{dy} + \sum_{n=1}^{N} V_n(t)\frac{dN_n^v(x.y)}{dx} - 2z\sum_{n=1}^{N} W_n(t)\frac{d^2N_n^w(x.y)}{dxy}\right. \\
& \left. + f(z)\sum_{n=1}^{N} X_n(t)\frac{dN_n^{\theta_1}(x.y)}{dy} + f(z)\sum_{n=1}^{N} Y_n(t)\frac{dN_n^{\theta_2}(x.y)}{dx}\right]^2 \\
& + \bar{Q}_{44}\left[f'(z)\sum_{n=1}^{N} Y_n(t)N_n^{\theta_2}(x.y)\right]^2 + \bar{Q}_{55}\left[f'(z)\sum_{n=1}^{N} X_n(t)N_n^{\theta_1}(x.y)\right]^2\Bigg)dV \\
& + \frac{2}{5}K_{imp}\big(y - w_0(a.b,t)\big)^{\frac{5}{2}}
\end{aligned}
\tag{15}
$$

$$
\begin{aligned}
T = \frac{1}{2}\int_V \rho\Bigg( & \left[\sum_{n=1}^{N} \frac{dU_n(t)}{dt}N_n^u(x.y) - z\sum_{n=1}^{N} \frac{dW_n(t)}{dt}\frac{dN_n^w(x.y)}{dx} + f(z)\sum_{n=1}^{N} \frac{dX_n(t)}{dt}N_n^{\theta_1}(x.y)\right]^2 \\
& + \left[\sum_{n=1}^{N} \frac{dV_n(t)}{dt}N_n^v(x.y) - z\sum_{n=1}^{N} \frac{dW_n(t)}{dt}\frac{dN_n^w(x.y)}{dy} + f(z)\sum_{n=1}^{N} \frac{dY_n(t)}{dt}N_n^{\theta_2}(x.y)\right]^2 \\
& + \left[\sum_{n=1}^{N} \frac{dW_n(t)}{dt}N_n^w(x.y)\right]^2\Bigg)dV + \frac{1}{2}M_{imp}\dot{y}^2
\end{aligned}
\tag{16}
$$

Motion equations can be determined based on the generalized Lagrange equations:

$$
\begin{aligned}
& \frac{d}{dt}\left(\frac{\partial T}{\partial \dot{U}_n}\right) - \frac{\partial T}{\partial U_n} + \frac{\partial P}{\partial U_n} = 0, \qquad n = 1,2,\dots,N \\
& \frac{d}{dt}\left(\frac{\partial T}{\partial \dot{V}_n}\right) - \frac{\partial T}{\partial V_n} + \frac{\partial P}{\partial V_n} = 0, \qquad n = 1,2,\dots,N \\
& \frac{d}{dt}\left(\frac{\partial T}{\partial \dot{W}_n}\right) - \frac{\partial T}{\partial W_n} + \frac{\partial P}{\partial W_n} = 0, \qquad n = 1,2,\dots,N \\
& \frac{d}{dt}\left(\frac{\partial T}{\partial \dot{X}_n}\right) - \frac{\partial T}{\partial X_n} + \frac{\partial P}{\partial X_n} = 0, \qquad n = 1,2,\dots,N \\
& \frac{d}{dt}\left(\frac{\partial T}{\partial \dot{Y}_n}\right) - \frac{\partial T}{\partial Y_n} + \frac{\partial P}{\partial Y_n} = 0, \qquad n = 1,2,\dots,N \\
& \frac{d}{dt}\left(\frac{\partial T}{\partial \dot{y}}\right) - \frac{\partial T}{\partial y} + \frac{\partial P}{\partial y} = 0
\end{aligned}
\tag{17}
$$

By substituting the eq. (15) and eq. (16) to eq. (17):

$$[M_{\mathrm{uu}}]\{\ddot{U}_n\}+[M_{\mathrm{uv}}]\{\ddot{V}_n\}+[M_{\mathrm{uw}}]\{\ddot{W}_n\}+\left[M_{u\theta_1}\right]\{\ddot{X}_n\}+\left[M_{u\theta_2}\right]\{\ddot{Y}_n\}+[K_{\mathrm{uu}}]\{U_n\}+[K_{\mathrm{uv}}]\{V_n\}+[K_{\mathrm{uw}}]\{W_n\}+\left[K_{u\theta_1}\right]\{X_n\}+\left[K_{u\theta_2}\right]\{Y_n\}=0$$

$$[M_{\mathrm{vu}}]\{\ddot{U}_n\}+[M_{\mathrm{vv}}]\{\ddot{V}_n\}+[M_{\mathrm{vw}}]\{\ddot{W}_n\}+\left[M_{v\theta_1}\right]\{\ddot{X}_n\}+\left[M_{v\theta_2}\right]\{\ddot{Y}_n\}+[K_{\mathrm{vu}}]\{U_n\}+[K_{\mathrm{vv}}]\{V_n\}+[K_{\mathrm{vw}}]\{W_n\}+\left[K_{v\theta_1}\right]\{X_n\}+\left[K_{v\theta_2}\right]\{Y_n\}=0$$

$$[M_{\mathrm{wu}}]\{\ddot{U}_n\}+[M_{\mathrm{wv}}]\{\ddot{V}_n\}+[M_{\mathrm{ww}}]\{\ddot{W}_n\}+\left[M_{w\theta_1}\right]\{\ddot{X}_n\}+\left[M_{w\theta_2}\right]\{\ddot{Y}_n\}+[K_{\mathrm{wu}}]\{U_n\}+[K_{\mathrm{wv}}]\{V_n\}+[K_{\mathrm{ww}}]\{W_n\}+\left[K_{w\theta_1}\right]\{\ddot{X}_n\}+\left[K_{w\theta_2}\right]\{Y_n\}=0 \tag{18}$$

$$\left[M_{\theta_1\mathrm{u}}\right]\{\ddot{U}_n\}+\left[M_{\theta_1\mathrm{v}}\right]\{\ddot{V}_n\}+\left[M_{\theta_1\mathrm{w}}\right]\{\ddot{W}_n\}+\left[M_{\theta_1\theta_1}\right]\{\ddot{X}_n\}+\left[M_{\theta_1\theta_2}\right]\{\ddot{Y}_n\}+\left[K_{\theta_1\mathrm{u}}\right]\{U_n\}+\left[K_{\theta_1\mathrm{v}}\right]\{V_n\}+\left[K_{\theta_1\mathrm{w}}\right]\{W_n\}+\left[K_{\theta_1\theta_1}\right]\{X_n\}+\left[K_{\theta_1\theta_2}\right]\{\ddot{Y}_n\}=0$$

$$\left[M_{\theta_2\mathrm{u}}\right]\{\ddot{U}_n\}+\left[M_{\theta_2\mathrm{v}}\right]\{\ddot{V}_n\}+\left[M_{\theta_2\mathrm{w}}\right]\{\ddot{W}_n\}+\left[M_{\theta_2\theta_1}\right]\{\ddot{X}_n\}+\left[M_{\theta_2\theta_2}\right]\{\ddot{Y}_n\}+\left[K_{\theta_2\mathrm{u}}\right]\{U_n\}+\left[K_{\theta_2\mathrm{v}}\right]\{V_n\}+\left[K_{\theta_2\mathrm{w}}\right]\{W_n\}+\left[K_{\theta_2\theta_1}\right]\{X_n\}+\left[K_{\theta_2\theta_2}\right]\{Y_n\}=0$$

In addition, by applying Newton's second law for contact force and considering Hertz's contact law, the Equilibrium equation can be expressed as

$$\ddot{y}=-F_{imp}\rightarrow m\ddot{y}=-K_{imp}\alpha^{3/2}=-K_{imp}\left(y-\sum_{n=1}^{N}W_n(t)N_n^w(a.b)\right) \tag{19}$$

Finally, nonlinear coupled time-dependent equations can be written as

$$\begin{bmatrix}[M_{\mathrm{uu}}] & [M_{\mathrm{uv}}] & [M_{\mathrm{uw}}] & \left[M_{u\theta_1}\right] & \left[M_{u\theta_2}\right]\\ [M_{\mathrm{vu}}] & [M_{\mathrm{vv}}] & [M_{\mathrm{vw}}] & \left[M_{v\theta_1}\right] & \left[M_{v\theta_2}\right]\\ [M_{\mathrm{wu}}] & [M_{\mathrm{wv}}] & [M_{\mathrm{ww}}] & \left[M_{w\theta_1}\right] & \left[M_{w\theta_2}\right]\\ \left[M_{\theta_1\mathrm{u}}\right] & \left[M_{\theta_1\mathrm{v}}\right] & \left[M_{\theta_1\mathrm{w}}\right] & \left[M_{\theta_1\theta_1}\right] & \left[M_{\theta_1\theta_2}\right]\\ \left[M_{\theta_2\mathrm{u}}\right] & \left[M_{\theta_2\mathrm{v}}\right] & \left[M_{\theta_2\mathrm{w}}\right] & \left[M_{\theta_2\theta_1}\right] & \left[M_{\theta_2\theta_2}\right]\end{bmatrix}\begin{Bmatrix}\{\ddot{U}_n\}\\ \{\ddot{V}_n\}\\ \{\ddot{W}_n\}\\ \{\ddot{X}_n\}\\ \{\ddot{Y}_n\}\end{Bmatrix}$$
$$+\begin{bmatrix}[K_{\mathrm{uu}}] & [K_{\mathrm{uv}}] & [K_{\mathrm{uw}}] & \left[K_{u\theta_1}\right] & \left[K_{u\theta_2}\right]\\ [K_{\mathrm{vu}}] & [K_{\mathrm{vv}}] & [K_{\mathrm{vw}}] & \left[K_{v\theta_1}\right] & \left[K_{v\theta_2}\right]\\ [K_{\mathrm{wu}}] & [K_{\mathrm{wv}}] & [K_{\mathrm{ww}}] & \left[K_{w\theta_1}\right] & \left[K_{w\theta_2}\right]\\ \left[K_{\theta_1\mathrm{u}}\right] & \left[K_{\theta_1\mathrm{v}}\right] & \left[K_{\theta_1\mathrm{w}}\right] & \left[K_{\theta_1\theta_1}\right] & \left[K_{\theta_1\theta_2}\right]\\ \left[K_{\theta_2\mathrm{u}}\right] & \left[K_{\theta_2\mathrm{v}}\right] & \left[K_{\theta_2\mathrm{w}}\right] & \left[K_{\theta_2\theta_1}\right] & \left[K_{\theta_2\theta_2}\right]\end{bmatrix}\begin{Bmatrix}\{U_n\}\\ \{V_n\}\\ \{W_n\}\\ \{X_n\}\\ \{Y_n\}\end{Bmatrix}=\begin{Bmatrix}0\\ 0\\ F_{imp}N_n^w(a.b)\\ 0\\ 0\end{Bmatrix} \tag{20}$$

The relation between the mass and stiffness components is mentioned in Appendix (A). Eq. (20) can be solved by as fourth-order Runge–Kutta numerical method. The initial conditions are

$$\begin{aligned}&U_n(0)=0,\ V_n(0)=0,\ W_n(0)=0,\ X_n(0)=0,\ Y_n(0)=0\\ &\dot{U}_n(0)=0,\ \dot{V}_n(0)=0,\ \dot{W}_n(0)=0,\ \dot{X}_n(0)=0,\ \dot{Y}_n(0)=0\\ &y(0)=0,\quad \dot{y(0)}=V_0\end{aligned} \tag{21}$$

## 3. Result and Discussion

To investigate the model, the FEM simulation is applied in the ABAQUS. The 937500 C3D8R element is used in the FEM model (Figure 2). Surface to Surface-to-surface contact is considered between the impactor and plate.

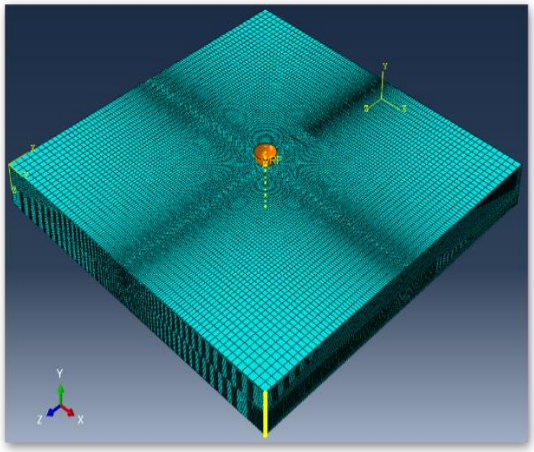

**Fig. 2.** FEM model of the LVI on the FG-CNTRC.

For validating the accuracy of the analytical model and FEM simulation, contact force and central deflection history computed by the analytical model and simulation are compared with Wang et al. model [19] as shown in Figure 3.

Table 1 shows the material and geometrical properties of the composite plate and the impactor used in Refs [15]. Figures 3(a) and 3(b) show a good agreement in the results.

Considering that the FEM simulation is based on solving the governing constitutive equations with the numerical method, but the analytical model presented in this paper is based on the third-order shear deformation Theory, Hertz contact law, and the energy principle, the difference between the results of the analytical model and the numerical method is greater than the difference between the results of the analytical model and Wang et al. model [19].

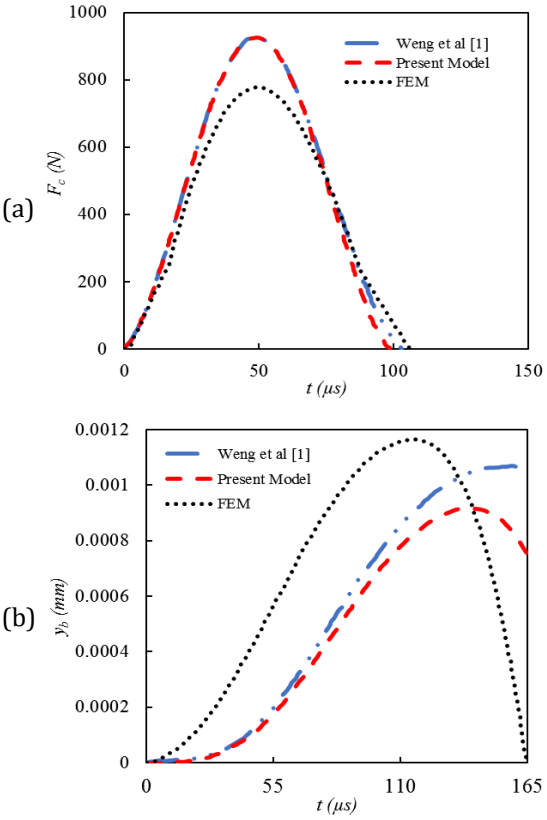


**Fig. 3.** Comparisons between the present model and FEM with Wang et al.model [20] for impact response of FG-X type of FG-CNTRC square plate: (a) contact force and (b) central deflection.

**Table 1.** Geometrical and material properties of FG-CNRTC Plate and impactor [15].

| |
|---|
| Geometrical properties of the plate |
| Simply supported boundary condition |
| Size: 200.0×200.0×20 mm |
| Mechanical properties of Poly (methyl methacrylate) |
| $E^m = 2.5GPa$ ; $\nu^m = 0.34$; $\rho^m = 1190\frac{kg}{m^3}$ |
| Mechanical properties of single-walled CNT (SWCNT) |
| $E_{11}^{CN} = 5.6466TPa$ ; $E_{22}^{CN} = 7.0800TPa$ ; |
| $G_{12}^{CN} = 1.9445TPa$ ; $\nu_{12}^{CN} = 0.175$ ; |
| $\rho^{CN} = 1400\frac{kg}{m^3}$ |
| properties of steel sphere impactor |
| $E^i = 207GPa$ ; $\nu^i = 0.3$ ; $\rho^i = 7960\frac{kg}{m^3}$ |
| Diameter= 12.7 mm |
| Velocity= 3 m/s |

### 3.1. Types of CNTRC Effects

In this section, the results of FG-CNTRC types (including UD, FG-V, FG-X, and FG-O) effects on the single-layer FG-CNTRC plate's contact force and central deflection are discussed. As shown in figure 4 (a), The volume fraction of CNT is equal to 0.28 ($V_{CN}^{*} = 0.28$). It is obvious from the figure, that the history of contact force of type X and V is similar together while the value of the maximum values of the contact force are equal to 925 and 926 *N* for the FG-CNTRC plate of type V and X, respectively. The behavior is due to enhancement of the volume fraction and $K_{imp}$ (Eq. (3)). Besides, the lowest contact time belongs to X and V types. FGO type has the maximum contact time and lowest contact force among other types of CNTs. From Figure 4 (b), It can be seen the FG-CNTRC plate of type X has the lowest deflection and shortest contact time duration.

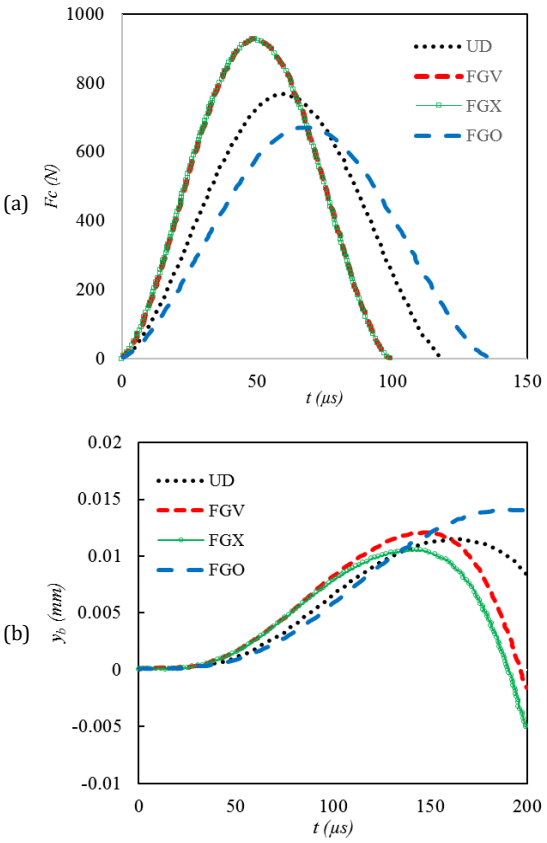


**Fig. 4.** Comparisons of impact response of four types of FG-CNTRC square plate: (a) contact force and (b) central deflection.

### 3.2. Volume Fraction of CNT Effects

The volume fraction of CNT is one of the effective parameters on the FG-CNTRC plate behavior under LVI.

In the section, the X type of FG-CNTRC plate is considered with different volume fractions ($V_{CN} = 0.12, 0.17, 0.28$). The effect on the contact force and central deflection are shown in Figure 5(a) and 5(b), respectively. According to the figure, by increasing the volume fraction the maximum value of the contact force is increased while contact time duration and central deflection are decreased. This response is due to the relation between $E_{22}$ and $V_{CN}$ (Eq. (10) so that enhancement of the $V_{CN}$ cause increasing of the $E_{22}$ and $K_{imp}$.

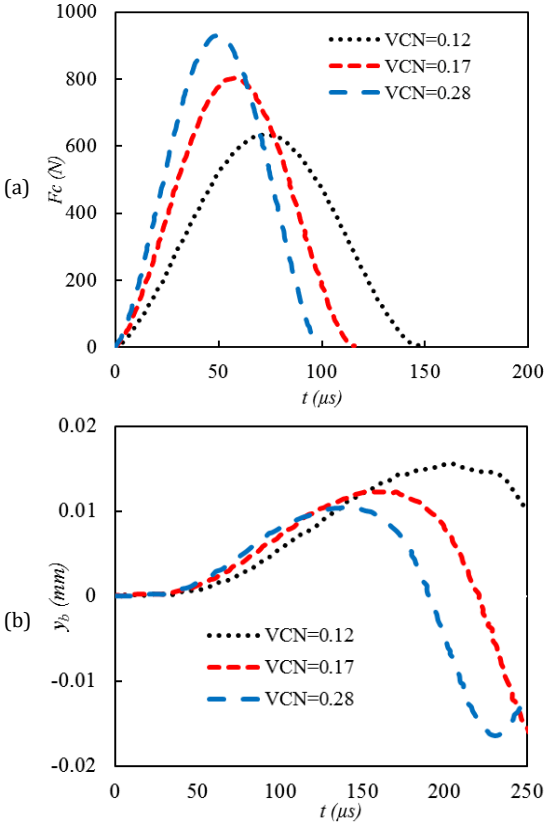


**Fig. 5.** Comparisons of impact response of volume fraction of X type of FG-CNTRC square plate: (a) contact force and (b) central deflection.

### 3.3. Effects of Initial Velocity

As illustrated in Eq.(2), the initial velocity of the impactor is an effective parameter of the kinetic energy of the system. The efficacy of initial velocity in the contact force and central deflection is shown in Figure 6. As seen from this figure (for three values of initial velocity 1,2 and 3 m/s), an increase in the initial velocity of the impactor, maximum value of contact force, and lower contact time duration are concluded. Besides, the central deflection of the plate increases as the initial velocity of the impactor increases.

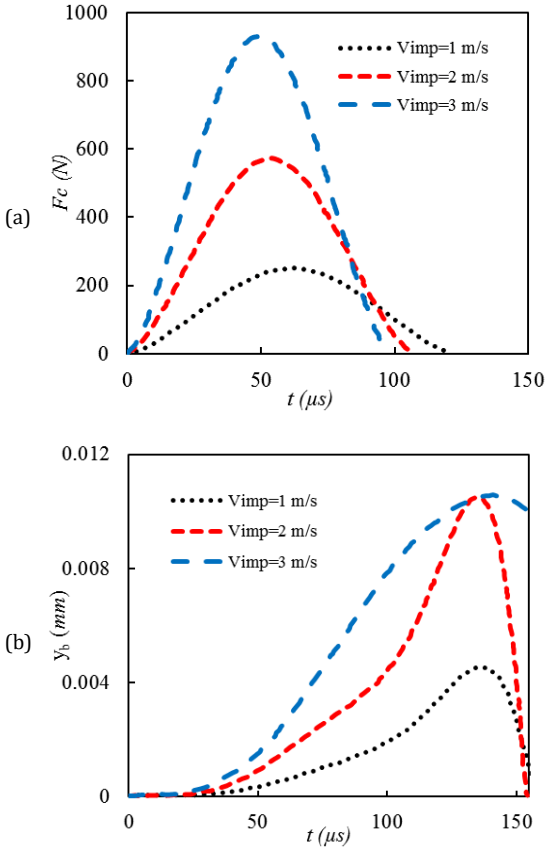


**Fig. 6.** Comparisons of impact response of volume fraction of X type of FG-CNTRC square plate with different initial velocities: (a) contact force and (b) central deflection.

### *3.4. Effects of Radius Impactor*

For the X type of FG-CNRTC, $V_0 = 3$ and different values of radius impactor ($R = 6.35, 9\ and\ 12\ mm$), the response of the plate under LVI is shown in Figure 7. It can be seen from the figure by increasing the radius impactor, the maximum value of the contact force and contact time duration increased. The central deflection of the plate is also increased by increasing the radius impactor. Enhancement of the impactor mass, which is due to increasing the radius, is the main reason for the plate response.

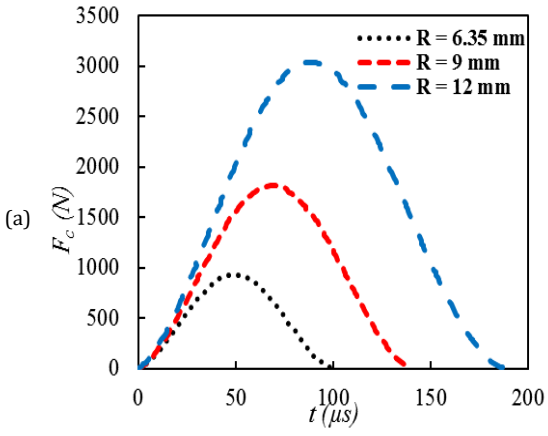


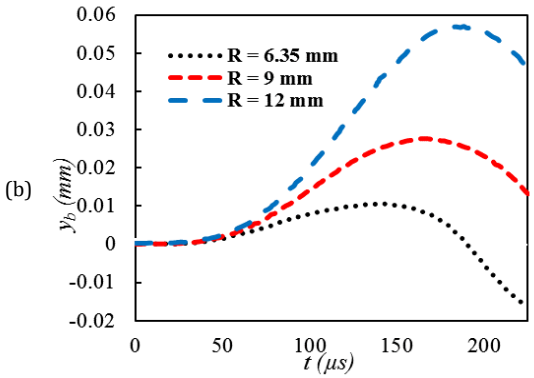


**Fig. 7.** Comparisons of impact response of volume fraction of X type of FG-CNTRC square plate with different radius impactors: (a) contact force and (b) central deflection.

## 4. Conclusions

In the paper, the behavior of an FG-CNTRC plate under Low-velocity impact (LVI) is investigated analytically and numerically. Properties of the plate are obtained by applying a rule of mixture. Hertz law and the energy principle are used to derive the governing equations of Third-order Shear Deformation Theory (TSDT). The Ritz method based on the linear functions is used to discrete the system's space domain equations of motion, which is solved by the fourth-order Runge-Kutta method. It is concluded that:

- Among the UD, FG-V, FG-X, and FG-O cases of CNT distribution, the FG-X, and FG-V types have the most contact force. Moreover, the FG-O type has the maximum contact time and lowest contact force among other types of CNTs.
- FG-X has the lowest deflection and shortest contact time duration.
- By increasing the volume fraction, the maximum value of the contact force is increased while contact time duration and central deflection are decreased.
- An increase in the initial velocity of the impactor, maximum value of contact force, and lower contact time duration are concluded
- The maximum value of the contact force and contact time duration increased by increasing the radius impactor.

## Acknowledgments

We would like to thank Razi University for supporting this research.

## Funding Statement

This research did not receive any specific grant from funding agencies in the public, commercial, or not-for-profit sectors.

## Conflicts of Interest

The author declares that there is no conflict of interest regarding the publication of this article.

## Appendix

The linear shape functions which are presented in Eq(14) are:

$$N_n^u(x.y) = x^{n-1}y^{n-1}L_uR_u$$

$$N_n^v(x.y) = x^{n-1}y^{n-1}L_vR_v$$

$$N_n^w(x.y) = x^{n-1}y^{n-1}L_wR_w \qquad \text{A(1)}$$

$$N_n^{\theta_1}(x.y) = x^{n-1}y^{n-1}L_{\theta_1}R_{\theta_1}$$

$$N_n^{\theta_2}(x.y) = x^{n-1}y^{n-1}L_{\theta_2}R_{\theta_2}$$

where $L$ and $R$ are dependent boundary conditions. For simple support:

$$@\ x = 0, a \rightarrow v_0 = w_0 = \theta_2 = 0$$
$$@\ y = 0, b \rightarrow u_0 = w_0 = \theta_1 = 0 \qquad \text{A(2)}$$

In the study, $L$ and $R$ are defined as below:

$$L_u = y, \quad R_u = b - y$$

$$L_v = x, \quad R_v = a - x$$

$$L_w = xy, \quad R_w = (a - x)(b - y) \qquad \text{A(3)}$$

$$L_{\theta_1} = y, \quad R_{\theta_1} = b - y$$

$$L_{\theta_2} = x, \quad R_{\theta_2} = a - x$$

The components of the mass and stiffness matrix can be calculated by the following equations:

$$M_{mn}^{uu} = \int_\Omega I_0 N_n^u N_m^u dxdy$$

$$M_{mn}^{uv} = 0$$

$$M_{mn}^{uw} = -\int_\Omega I_1 N_{n.x}^w N_m^u dxdy$$

$$M_{mn}^{u\theta_1} = \int_\Omega I_{f0} N_n^{\theta_1} N_m^u dxdy$$

$$M_{mn}^{u\theta_2} = 0$$

$$M_{mn}^{vu} = 0$$

$$M_{mn}^{vv} = \int_\Omega I_0 N_n^v N_m^v dxdy$$

$$M_{mn}^{vw} = -\int_\Omega I_1 N_{n.y}^v N_m^v dxdy$$

$$M_{mn}^{v\theta_1} = 0$$

$$M_{mn}^{v\theta_2} = \int_\Omega I_{f0} N_n^{\theta_2} N_m^v dxdy$$

$$M_{mn}^{wu} = -\int_\Omega I_1 N_n^v N_{m.x}^w dxdy$$

$$M_{mn}^{wv} = -\int_\Omega I_1 N_n^v N_{m.y}^w dxdy$$

$$M_{mn}^{ww} = \int_\Omega \left(I_0 N_n^w N_m^w + I_2 N_{n.x}^w N_{m.x}^w + I_2 N_{n.y}^w N_{m.y}^w\right) dxdy$$

$$M_{mn}^{w\theta_1} = -\int_\Omega I_{f1} N_n^{\theta_1} N_{m.x}^w dxdy$$

$$M_{mn}^{w\theta_2} = -\int_\Omega I_{f1} N_n^{\theta_2} N_{m.y}^w dxdy$$

$$M_{mn}^{\theta_1 u} = \int_\Omega I_{f0} N_n^u N_m^{\theta_1} dxdy$$

$$M_{mn}^{\theta_1 v} = 0$$

$$M_{mn}^{\theta_1 u} = -\int_\Omega I_{f1} N_{n.x}^w N_m^{\theta_1} dxdy$$

$$M_{mn}^{\theta_1\theta_1} = \int_\Omega I_{ff} N_n^{\theta_1} N_m^{\theta_1} dxdy$$

$$M_{mn}^{\theta_1\theta_2} = \int_\Omega I_{f0} N_n^u N_m^{\theta_1} dxdy$$

$$M_{mn}^{\theta_2 u} = 0$$

$$M_{mn}^{\theta_2 v} = \int_{\Omega} I_{f0} N_n^v \, N_m^{\theta_2} dxdy$$

$$M_{mn}^{\theta_2 w} = -\int_{\Omega} I_{f1} N_{n.y}^w \, N_m^{\theta_2} dxdy$$

$$M_{mn}^{\theta_2 \theta_1} = 0$$

$$M_{mn}^{\theta_2 \theta_2} = \int_{\Omega} I_{ff} N_n^{\theta_2} \, N_m^{\theta_2} dxdy \qquad \text{A(4)}$$

$$\begin{Bmatrix} I_0 \\ I_1 \\ I_2 \\ I_{f0} \\ I_{f1} \\ I_{ff} \end{Bmatrix} = \int_{-\frac{h}{2}}^{\frac{h}{2}} \rho_0 \begin{Bmatrix} 1 \\ z \\ z^2 \\ f(z) \\ zf(z) \\ \left(f(z)\right)^2 \end{Bmatrix} dz$$

$$K_{mn}^{uu} = \int_{\Omega} \left( A_{11} N_{n.x}^u N_{m.x}^u + A_{16} N_{n.y}^u N_{m.x}^u + A_{16} N_{n.x}^u N_{m.y}^u + A_{66} N_{n.y}^u N_{m.y}^u \right) dxdy$$

$$K_{mn}^{uv} = \int_{\Omega} \left( A_{12} N_{n.y}^v N_{m.x}^u + A_{16} N_{n.x}^v N_{m.x}^u + A_{26} N_{n.y}^v N_{m.y}^u + A_{66} N_{n.x}^v N_{m.y}^u \right) dxdy$$

$$K_{mn}^{uw} = -\int_{\Omega} \left( B_{11} N_{n.xx}^w N_{m.x}^u + B_{12} N_{n.yy}^w N_{m.x}^u + 2B_{16} N_{n.xy}^w N_{m.x}^u + B_{16} N_{n.xx}^w N_{m.y}^u + B_{26} N_{n.yy}^w N_{m.y}^u + 2B_{66} N_{n.xy}^w N_{m.y}^u \right) dxdy$$

$$K_{mn}^{u\theta_1} = \int_{\Omega} \left( E_{11} N_{n.x}^{\theta_1} N_{m.x}^u + E_{16} N_{n.y}^{\theta_1} N_{m.x}^u + E_{66} N_{n.y}^{\theta_1} N_{m.y}^u + E_{16} N_{n.x}^{\theta_1} N_{m.y}^u \right) dxdy$$

$$K_{mn}^{u\theta_2} = \int_{\Omega} \left( E_{12} N_{n.y}^{\theta_2} N_{m.x}^u + E_{16} N_{n.x}^{\theta_2} N_{m.x}^u + E_{26} N_{n.y}^{\theta_2} N_{m.y}^u + E_{66} N_{n.x}^{\theta_2} N_{m.y}^u \right) dxdy$$

$$K_{mn}^{vu} = \int_{\Omega} \left( A_{12} N_{n.x}^u N_{m.y}^v + A_{26} N_{n.y}^u N_{m.y}^v + A_{16} N_{n.x}^u N_{m.x}^v + A_{66} N_{n.y}^u N_{m.x}^v \right) dxdy$$

$$K_{mn}^{vv} = \int_{\Omega} \left( A_{22} N_{n.y}^v N_{m.y}^v + A_{26} N_{n.x}^v N_{m.y}^v + A_{26} N_{n.y}^v N_{m.x}^v + A_{66} N_{n.x}^v N_{m.x}^v \right) dxdy$$

$$K_{mn}^{vw} = -\int_{\Omega} \left( B_{12} N_{n.xx}^w N_{m.y}^v + B_{22} N_{n.yy}^w N_{m.y}^v + 2B_{26} N_{n.xy}^w N_{m.y}^v + B_{16} N_{n.xx}^w N_{m.x}^v + B_{26} N_{n.yy}^w N_{m.x}^v + 2B_{66} N_{n.xy}^w N_{m.x}^v \right) dxdy$$

$$K_{mn}^{v\theta_1} = \int_{\Omega} \left( E_{12} N_{n.x}^{\theta_1} N_{m.y}^v + E_{26} N_{n.y}^{\theta_1} N_{m.y}^v + E_{66} N_{n.y}^{\theta_1} N_{m.x}^u + E_{16} N_{n.x}^{\theta_1} N_{m.y}^u \right) dxdy$$

$$K_{mn}^{v\theta_2} = \int_{\Omega} \left( E_{22} N_{n.y}^{\theta_2} N_{m.x}^v + E_{26} N_{n.x}^{\theta_2} N_{m.y}^v + E_{26} N_{n.y}^{\theta_2} N_{m.x}^v + E_{66} N_{n.x}^{\theta_2} N_{m.x}^v \right) dxdy$$

$$K_{mn}^{wu} = -\int_{\Omega} \left( B_{11} N_{n.x}^u N_{m.xx}^w + B_{12} N_{n.x}^u N_{m.yy}^w + B_{16} N_{n.y}^u N_{m.xx}^w + 2B_{16} N_{n.x}^u N_{m.xy}^w + B_{26} N_{n.y}^u N_{m.yy}^w + 2B_{66} N_{n.y}^u N_{m.xy}^w \right) dxdy$$

$$K_{mn}^{wv} = -\int_{\Omega} \left( B_{12} N_{n.y}^v N_{m.xx}^w + B_{16} N_{n.x}^v N_{m.xx}^w + B_{22} N_{n.y}^v N_{m.yy}^w + B_{26} N_{n.x}^v N_{m.yy}^w + 2B_{26} N_{n.y}^v N_{m.xy}^w + 2B_{66} N_{n.x}^v N_{m.xy}^w \right) dxdy$$

$$K_{mn}^{ww} = -\int_{\Omega} \left(D_{11}N_{n.xx}^{w}N_{m.xx}^{w} + D_{12}N_{n.yy}^{w}N_{m.xx}^{w} + 2D_{16}N_{n.xy}^{w}N_{m.xx}^{w} + D_{12}N_{n.xx}^{w}N_{m.yy}^{w} + D_{22}N_{n.yy}^{w}N_{m.yy}^{w} + 2D_{26}N_{n.xy}^{w}N_{m.yy}^{w} + 2D_{16}N_{n.xx}^{w}N_{m.xy}^{w} + 2D_{26}N_{n.yy}^{w}N_{m.xy}^{w} + 4D_{66}N_{n.xy}^{w}N_{m.xy}^{w}\right)dxdy$$

$$K_{mn}^{w\theta_1} = -\int_{\Omega} \left(F_{11}N_{n.x}^{\theta_1}N_{m.xx}^{w} + F_{16}N_{n.y}^{\theta_1}N_{m.xx}^{w} + F_{12}N_{n.x}^{\theta_1}N_{m.yy}^{w} + F_{26}N_{n.y}^{\theta_1}N_{m.yy}^{w} + 2F_{16}N_{n.x}^{\theta_1}N_{m.xy}^{w} + 2F_{66}N_{n.y}^{\theta_1}N_{m.xy}^{w}\right)dxdy$$

$$K_{mn}^{w\theta_2} = -\int_{\Omega} \left(F_{12}N_{n.y}^{\theta_2}N_{m.xx}^{w} + F_{16}N_{n.x}^{\theta_2}N_{m.xx}^{w} + F_{22}N_{n.y}^{\theta_2}N_{m.yy}^{w} + F_{26}N_{n.x}^{\theta_2}N_{m.yy}^{w} + 2F_{26}N_{n.y}^{\theta_2}N_{m.xy}^{w} + 2F_{66}N_{n.x}^{\theta_2}N_{m.xy}^{w}\right)dxdy$$

$$K_{mn}^{\theta_1 u} = \int_{\Omega} \left(E_{11}N_{n.x}^{u}N_{m.x}^{\theta_1} + E_{16}N_{n.y}^{u}N_{m.x}^{\theta_1} + E_{16}N_{n.x}^{u}N_{m.y}^{\theta_1} + E_{66}N_{n.y}^{u}N_{m.y}^{\theta_1}\right)dxdy$$

$$K_{mn}^{\theta_1 v} = \int_{\Omega} \left(E_{12}N_{n.y}^{v}N_{m.x}^{\theta_1} + E_{16}N_{n.x}^{v}N_{m.x}^{\theta_1} + E_{26}N_{n.y}^{v}N_{m.y}^{\theta_1} + E_{66}N_{n.x}^{v}N_{m.y}^{\theta_1}\right)dxdy$$

$$K_{mn}^{\theta_1 w} = -\int_{\Omega} \left(F_{11}N_{n.xx}^{w}N_{m.x}^{\theta_1} + F_{12}N_{n.yy}^{w}N_{m.x}^{\theta_1} + 2F_{16}N_{n.xy}^{w}N_{m.x}^{\theta_1} + F_{16}N_{n.xx}^{w}N_{m.y}^{\theta_1} + F_{26}N_{n.yy}^{w}N_{m.y}^{\theta_1} + 2F_{66}N_{n.xy}^{w}N_{m.y}^{\theta_1}\right)dxdy$$

$$K_{mn}^{\theta_1\theta_1} = \int_{\Omega} \left(H_{11}N_{n.x}^{\theta_1}N_{m.x}^{\theta_1} + H_{16}N_{n.y}^{\theta_1}N_{m.x}^{\theta_1} + H_{16}N_{n.y}^{\theta_1}N_{m.y}^{\theta_1} + H_{66}N_{n.y}^{\theta_1}N_{m.y}^{\theta_1} + J_{55}N_{n}^{\theta_1}N_{m}^{\theta_1}\right)dxdy$$

$$K_{mn}^{\theta_1\theta_2} = \int_{\Omega} \left(H_{12}N_{n.y}^{\theta_2}N_{m.x}^{\theta_1} + H_{16}N_{n.x}^{\theta_2}N_{m.x}^{\theta_1} + H_{26}N_{n.y}^{\theta_2}N_{m.y}^{\theta_1} + H_{66}N_{n.x}^{\theta_2}N_{m.y}^{\theta_1}\right)dxdy$$

$$K_{mn}^{\theta_2 u} = \int_{\Omega} \left(E_{12}N_{n.x}^{u}N_{m.x}^{\theta_2} + E_{26}N_{n.y}^{u}N_{m.x}^{\theta_2} + E_{16}N_{n.x}^{u}N_{m.y}^{\theta_2} + E_{66}N_{n.y}^{u}N_{m.x}^{\theta_2}\right)dxdy$$

$$K_{mn}^{\theta_2 v} = \int_{\Omega} \left(E_{22}N_{n.y}^{v}N_{m.x}^{\theta_2} + E_{26}N_{n.x}^{v}N_{m.x}^{\theta_2} + E_{26}N_{n.y}^{v}N_{m.y}^{\theta_2} + E_{66}N_{n.x}^{v}N_{m.x}^{\theta_2}\right)dxdy$$

$$K_{mn}^{\theta_2 w} = -\int_{\Omega} \left(F_{12}N_{n.xx}^{w}N_{m.y}^{\theta_2} + F_{22}N_{n.yy}^{w}N_{m.y}^{\theta_2} + 2F_{26}N_{n.xy}^{w}N_{m.y}^{\theta_2} + F_{16}N_{n.xx}^{w}N_{m.x}^{\theta_2} + F_{26}N_{n.yy}^{w}N_{m.x}^{\theta_2} + 2F_{66}N_{n.xy}^{w}N_{m.x}^{\theta_2}\right)dxdy$$

$$K_{mn}^{\theta_2\theta_1} = \int_{\Omega} \left(H_{12}N_{n.x}^{\theta_1}N_{m.y}^{\theta_2} + H_{26}N_{n.y}^{\theta_1}N_{m.y}^{\theta_2} + H_{16}N_{n.x}^{\theta_1}N_{m.x}^{\theta_2} + H_{66}N_{n.y}^{\theta_1}N_{m.x}^{\theta_2}\right)dxdy$$

$$K_{mn}^{\theta_2\theta_2} = \int_{\Omega} \left(H_{22}N_{n.y}^{\theta_2}N_{m.y}^{\theta_2} + H_{26}N_{n.y}^{\theta_2}N_{m.x}^{\theta_2} + H_{26}N_{n.x}^{\theta_2}N_{m.y}^{\theta_2} + H_{66}N_{n.x}^{\theta_2}N_{m.x}^{\theta_2} + +J_{44}N_{n}^{\theta_2}N_{m}^{\theta_2}\right)dxdy \qquad \text{A(5)}$$

$$\begin{Bmatrix} A_{ij} \\ B_{ij} \\ D_{ij} \\ E_{ij} \\ F_{ij} \\ H_{ij} \end{Bmatrix} = \sum_{k=1}^{n} \int_{z_k}^{z_{k+1}} \bar{Q}_{ij}^{k} \begin{Bmatrix} 1 \\ z \\ z^2 \\ f(z) \\ zf(z) \\ (f(z))^2 \end{Bmatrix} dz \quad i.j = 1.2.6$$

$$J_{ij} = \sum_{k=1}^{n} \int_{z_k}^{z_{k+1}} \bar{Q}_{ij}^{k} \left(f'(z)\right)^2 dz \qquad i.j = 4.5$$

## References


[1] Jam, J.E. & Kiani, Y., 2015. Low velocity impact response of functionally graded carbon nanotube reinforced composite beams in thermal environment. *Composite Structures, 132*, pp.35-43.

[2] Yang, C.-H., Ma, W.-N., Ma, D.-W., He, Q. & Zhong, J.-L., 2018. Analysis of the low velocity impact response of functionally graded carbon nanotubes reinforced composite spherical shells. *Journal of Mechanical Science and Technology, 32* (6), pp.2681-2691.

[3] Cuomo, S., Bätzel, T., Modler, N., Hornig, A. & Meo, M., 2022. High velocity impact on generic cfrp blade specimen: Baseline free method for impact localisation and damage assessment on complex structures. *Smart Materials and Structures, 31* (6), pp.065024.

[4] Alonso, L. & Solis, A., 2021. High-velocity impact on composite sandwich structures: A theoretical model. *International Journal of Mechanical Sciences, 201*, pp.106459.

[5] Jafari, S.S., Majzoobi, G.H., Khademi, E. & Kashfi, M., 2019. Development of a new technique for measuring damage accumulation at high strain rates. *Engineering Fracture Mechanics, 209*, pp.162-172.

[6] Zhang, K., Cao, Y., An, J. & Wang, K., 2021. Viscoplastic behavior of aa7075 aluminum alloy at high strain rate. *Journal of Mechanical Science and Technology, 35* (12), pp.5405-5413.

[7] Taghipoor, H., Fereidoon, A., Ghasemi-Ghalebahman, A. & Mirzaei, J., 2023. Experimental assessment of mechanical behavior of basalt/graphene/pp-g-ma-reinforced polymer nanocomposites by response surface methodology. *Polymer Bulletin, 80* (7), pp.7663-7685.

[8] Taghipoor, H. & Mirzaei, J., 2023. Statistical predicting and optimization of the tensile properties of natural fiber bio-composites. *Polymer Bulletin*, pp.1-25.

[9] Sadeghian, A., Moradi Shaghaghi, T., Mohammadi, Y. & Taghipoor, H., 2023. Performance assessment of hybrid fibre-reinforced concrete (frc) under low-speed impact: Experimental analysis and optimized mixture. *Shock and Vibration, 2023*.

[10] Zarei, H., Fallah, M., Minak, G., Bisadi, H. & Daneshmehr, A., 2016. Low velocity impact analysis of fiber metal laminates (fmls) in thermal environments with various boundary conditions. *Composite Structures, 149*, pp.170-183.

[11] Lei, Z.X. & Tong, L.H., 2019. Analytical solution of low-velocity impact of graphene-reinforced composite functionally graded cylindrical shells. *Journal of the Brazilian Society of Mechanical Sciences and Engineering, 41* (11), pp.486.

[12] Fallah, M., Daneshmehr, A., Zarei, H., Bisadi, H. & Minak, G., 2018. Low velocity impact modeling of functionally graded carbon nanotube reinforced composite (fg-cntrc) plates with arbitrary geometry and general boundary conditions. *Composite Structures, 187*, pp.554-565.

[13] Feli, S., Karami, L. & Jafari, S.S., 2019. Analytical modeling of low velocity impact on carbon nanotube-reinforced composite (cntrc) plates. *Mechanics of Advanced Materials and Structures, 26* (5), pp.394-406.

[14] Yang, C. & Ma, W., 2022. Low-velocity impact response of fg-cntrc laminated plates with negative poisson's ratios and clamped boundary conditions. *Journal of the Brazilian Society of Mechanical Sciences and Engineering, 44* (8), pp.1-13.

[15] Wang, Z.-X., Xu, J. & Qiao, P., 2014. Nonlinear low-velocity impact analysis of temperature-dependent nanotube-reinforced composite plates. *Composite Structures, 108*, pp.423-434.

[16] Reddy, J.N., 2003. *Mechanics of laminated composite plates and shells: Theory and analysis*. CRC press.

[17] Alihemmati, J., Tadi Beni, Y., Soltanimaleki, A. & Nejati, M., 2021. Frequency analysis of functionally graded carbon nanotube-reinforced cylindrical panels by mesh-free galerkin method. *Mechanics Of Advanced Composite Structures, 8* (2), pp.415-424.

[18] Rashidi, M.M., Bagheri, S., Momoniat, E. & Freidoonimehr, N., 2017. Entropy analysis of convective mhd flow of third grade non-newtonian fluid over a stretching sheet. *Ain Shams Engineering Journal, 8* (1), pp.77-85.

[19] Yas, M.H. & Afshin, S., 2021. Effect of general thermal boundary conditions on

the dynamic and buckling of polymeric hybrid nanocomposite beam with variable thickness. *Journal of The Institution of Engineers (India): Series C, 102* (2)**,** pp.305-321.

[20] Soni, S.K., Thomas, B., Swain, A. & Roy, T., 2022. Functionally graded carbon nanotubes reinforced composite structures: An extensive review. *Composite Structures, 299***,** pp.116075.